Rev. Roum. Sci. Techn.– Électrotechn. et Énerg.
Vol. **70**, *3*, pp. 409–414, Bucarest, 2025

HEAT RECOVERY DURING BIOMASS PYROLYSIS PROVIDED WITH A THERMOELECTRIC METAL PLATE-BASED SYSTEM

HERVÉ KLINKLIN BADAKA[1, *], DAMGOU MANI KONGNINE [2], ALEXANDRU M. MOREGA [3]

Keywords: Biomass pyrolysis; Numerical simulation; Heat recovery; Thermoelectric module; Hot air drying.

This work presents a numerical study of wood pyrolysis in a parallelepiped carbonizer equipped with a chimney and clay insulation to enhance charcoal yield. A thermal energy recovery system, consisting of six steel plates connected by five rods, was integrated to explore the potential for electricity generation. Simulation results indicate that the chimney exhaust temperature reaches approximately 350 K, making it suitable for drying or biomass preheating. The hot side of the final plate, intended to host a thermoelectric module, can reach a temperature of up to 443 K. Under these conditions, the TEG1-PB-12611-6.0 module can generate up to 3.97 W.

1. INTRODUCTION

In the face of the energy crisis and global warming, biomass valorization is emerging as a promising solution [1]. Pyrolysis allows for the production of charcoal from agroforestry waste, but its yield strongly depends on the proper design of the carbonization device. Understanding the physical and chemical phenomena involved is therefore essential [2].

The heat released during carbonization can be recovered for other uses (drying, preheating, electricity generation). This study models a parallelepiped carbonization device incorporating a heat recovery system made of steel plates and rods. The objective is to simulate pyrolysis and thermomechanical transfers to optimize the system's configuration. Finally, based on the characteristics of a commercially available thermoelectric module (TEG1-PB-12611-6.0 an estimate of the maximum electrical power that the device can generate will be provided.

2. PRESENTATION OF THE DEVICE STUDIED NUMERICALLY

Figure 1 illustrates the FEM computational domain.

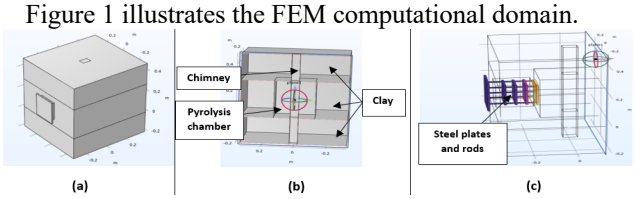

Fig. 1 – Geometry of the carbonizer: (a) 3D model; (b) 2D clipping model (front); 2D clipping model (profile).

The pyrolyzer chamber measures 31 cm in length, 25 cm in width, and 28 cm in height, with a total volume of 21.7 l. It's insulated with 20 cm of clay to reduce heat loss and maintain temperature [3]. The system includes a 68 cm tall, 7 cm × 5 cm cross-section chimney for gas release and pressure regulation [4]. Six steel plates (14 cm × 14 cm × 0.3 cm), connected by five 23 cm steel rods, recover heat; their air gaps insulate and lower temperatures to safe levels (633 K) for thermoelectric modules [5], preventing damage from the chamber, which can reach 773 K [6].

3. MATHEMATICAL MODEL

3.1. THE PYROLYSIS CHAMBER

The COMSOL physical interfaces used to model this compartment will be presented.

3.1.1. REACTION SCHEME

Carbonization is a thermochemical process that occurs between 673 K and 873 K, with minimal oxygen, producing charcoal, tar, and gases [7]. In this study, wood decomposes into these products, with tar further breaking down into more gas and char. Initially described by Shafizadeh et al. [8], this model was later adapted by Blasi for wood pyrolysis modeling [9].

The mass source term Q_m $\left[\frac{\text{kg}}{\text{m}^3\cdot\text{s}}\right]$and the heat source term $\dot{Q}$ $\left[\frac{\text{W}}{\text{m}^3}\right]$, which represent respectively the generation of volatiles and the heat exchange during the pyrolysis, are derived from the reaction scheme shown in Fig. 2.

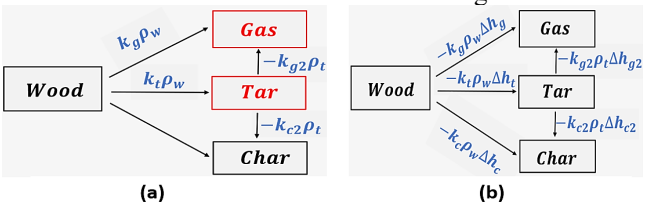

Fig. 2 – Contribution of Chemical Species to the: (a) mass source term; (b) heat source term.

Thus, the mass source term is given by:

$$Q_m = k_t\rho_w + k_g\rho_w - (k_{c2}+k_{g2})\rho_t, \quad (1)$$

and the heat source term is:

$$\dot{Q} = -\left(k_t\Delta h_t + k_g\Delta h_g + k_c\Delta h_c\right)\rho_w - (k_{g2}\Delta h_{g2} + k_{c2}\Delta h_{c2})\rho_t. \quad (2)$$

The Arrhenius equation provides the temperature dependence of reaction rates:

$$k_i = A_i e^{-\frac{E_i}{RT}}. \quad (3)$$

In this model, k_i [s^{-1}] denotes the reaction rate constant, A_i [s^{-1}] is the pre-exponential factor, and E_i [J/mol] represents the activation energy.

The kinetic parameters, along with the corresponding reaction enthalpies, are presented in Table 1. The term Δh_i [kJ/kg] indicates the heat associated with each pyrolysis reaction.

Table 1

Model kinetics parameters and heats of pyrolysis [10].

Reaction	A_i [s^{-1}]	E_i [J/mol]	Δh_i [kJ/kg]
c	$3.27\cdot10^6$	11,700	64
t	$1.08\cdot10^{10}$	148,000	64
g	$4.38\cdot10^9$	152,700	64
c2	$1.00\cdot10^5$	108,000	-42
g2	$4.28\cdot10^6$	108,000	-42

[1, *] Regional Center of Excellence for Electricity Control (CERME), University of Lome, Lome 01 BP 1515, Togo. (Correspondence)
[2] Faculty of Sciences, Department of Physics, Solar Energy Laboratory, University of Lome, Lome 01 BP 1515, Togo.
[3] Faculty of Electrical Engineering, National University of Science and Technology Politehnica Bucharest, Romania.
E-mails : herve.badaka@gmail.com, kongnine@gmail.com, alexandru.morega@upb.

DOI: 10.59277/RRST-EE.2025.70.3.21

3.1.2. DARCY'S LAW

During biomass carbonization, gases and tar are produced and flow slowly through the porous bed [11]. This flow is modeled using Darcy's law, assuming laminar, incompressible, single-phase flow:

$$\frac{\mathrm{d}\rho_f}{\mathrm{d}t} + \nabla \cdot (\rho_f \mathbf{u}) = Q_m, \tag{4}$$

where the ideal gas law gives the fluid density:

$$\rho_f = \frac{P\left(\sum_k \frac{\omega_k}{M_k}\right)^{-1}}{RT}. \tag{5}$$

Here ω_i is the mass fraction of gaseous species *i* (gas, tar, air) and M_i [kg/mol], their molar weight, which are respectively 0.038, 0.11, and 0.029. R = 8.314 J/(K·mol) represents the universal ideal gas constant. The relation:

$$\mathbf{u} = -\frac{\kappa}{\mu}\nabla P, \tag{6}$$

provides Darcy's velocity, where $\kappa = 5{\cdot}10^{-16}$ m^2 is the effective permeability of the biomass bed; $\mu = 3{\cdot}10^{-5}$ kg/(m·s) is the dynamic viscosity of the gas mixture, and ∇P [Pa/m] is the pressure gradient—using eq. (4) to (6), the mass conservation can be rewritten in terms of pressure, temperature, and mass fraction.

$$\frac{\mathrm{d}P}{\mathrm{d}t} + \nabla \cdot \left(-\frac{\kappa}{M} P \nabla P\right) = \frac{Q_m}{\frac{P\left(\sum_k \frac{\omega_k}{M_k}\right)^{-1}}{RT}}. \tag{7}$$

The initial pressure is $P_0 = 0$, relative to the reference pressure, P = 1 atm.

For the chimney holes, the boundary condition is given by the law of Hagen-Poiseuille [12]:

$$\dot{m}_{surface} = -N\rho\frac{\pi r^4}{8\mu LA}P, \tag{8}$$

where N = 6 holes on each wall surface A (m²); $L = 3{\cdot}10^{-3}$ m is the length of the hole, each with radius $r = 6{\cdot}10^{-3}$ m, and P [Pa] is the pressure at the inlet of the hole. Thus, for the wall 28 cm x 7 cm and the wall 28 cm x 5 cm $\dot{m}_1 = -0.613\ [\mathrm{kg}/(\mathrm{s}\cdot\mathrm{Pa}]\cdot P$, respectively $\dot{m}_2 = -0.858\ [\mathrm{kg}/(\mathrm{s}\cdot\mathrm{Pa}]\cdot P$, (Fig. 3). For the other boundaries, zero flux: $-\mathbf{n}\cdot\rho\mathbf{u} = 0$.

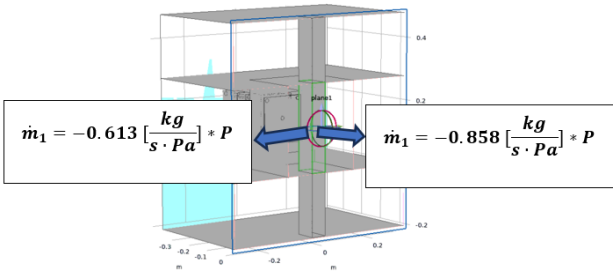

Fig. 3 – Mass flux exchange between pyrolysis chamber and chimney.

The pressure diffusion time constant is $\tau_1 = \frac{L^2\mu}{\kappa P_0} = 46.44$ s.

3.1.3. TRANSPORT OF CONCENTRATED SPECIES IN POROUS MEDIA

This interface models the movement of volatile gases in the pyrolysis chamber, including convection, diffusion, and chemical reactions. The mass conservation equation for the volatile species *i* (pyrolysis gases, tar, and air) is:

$$\varepsilon\rho_f\frac{\partial\omega_i}{\partial t} + \nabla\cdot\mathbf{J_i} + \rho_f(\boldsymbol{u_t}\cdot\nabla)\omega_i = R_i, \tag{9}$$

where $\mathbf{J}_i$ is the diffusion flux described by Flick's law:

$$\mathbf{J_i} = -\rho_f\left(\varepsilon^{\frac{4}{3}}D_i\nabla\omega_i - \omega_i\sum_k D_k\nabla\omega_k)\right). \tag{10}$$

Where $D_i = \frac{10^{-5}m^2}{s}$ are diffusivities and ε = 0.3 the porosity of the domain and $R_i\left[\frac{\mathrm{kg}}{\mathrm{m^3\cdot s}}\right]$ is the generation term source for the specie *i* with:

$$\begin{cases} R_{tar} = \rho_f\frac{\partial\omega_t}{\partial t} = k_t\rho_w - (k_{c2} + k_{g2})\rho\omega_t, \\ \mathrm{R_gas} = \rho_f\frac{\partial\omega_g}{\partial t} = k_g\rho_w + k_{g2}\rho\omega_t. \\ \mathrm{R_{air}} = 0. \end{cases} \tag{11}$$

To model the incoming airflow that supports the carbonization process, we define the total velocity as $\mathbf{u}_t = \mathbf{u} + \mathbf{u}_{air}$, where $\mathbf{u}$ is Darcy's velocity and $\mathbf{u}_{air}$ the air inlet velocity prescribed as: $|\mathbf{u}_{air}| = 0.05\frac{\mathrm{m}}{\mathrm{s}}$.

Initially, only air is present in the pyrolysis chamber $\omega_{g,0} = 0;\ \omega_{t,0} = 0;\ \omega_{a,0} = 1$.

It is assumed that there is no outward diffusive flux at the domain boundary $\mathbf{n}\cdot\mathbf{J_i} = 0$.

The characteristic transport times were estimated for mass transfer. The diffusion time constant is $\tau_{2d} = \frac{L^2}{\frac{1}{\varepsilon^{\frac{4}{3}}D_i}} = 1.06\cdot 10^4\ s$, while the convection time is $\tau_{2c} = \frac{\varepsilon L}{u_t} = 2.24$ s. Since $\tau_{2c} \ll \tau_{2d}$convective transport dominates over diffusive effects in species migration.

3.1.4. HEAT TRANSFER IN POROUS MEDIA

This phenomenon is modeled using the Heat Transfer in Porous Media physics interface, which formulates the governing equation under transient conditions as follows:

$$(\rho C_P)_{\mathrm{eff}}\frac{\partial T}{\partial t} + \nabla\cdot(-k_{\mathrm{eff}}\nabla T) + \rho_f C_{p,f}(\mathbf{u}\cdot\nabla)T = \dot{Q}, \tag{12}$$

$$(\rho C_P)_{\mathrm{eff}} = \varepsilon\rho_f C_{p,f} + \rho_b\left(\frac{C_{p,w}\rho_w + C_{p,c}\rho_c}{\rho_{w,0}}\right). \tag{13}$$

The effective thermal conductivity is

$$k_{\mathrm{eff}} = \varepsilon k_f + \left(\frac{k_w\rho_w + k_c\rho_c}{\rho_{w,0}}\right) + \frac{13.5\sigma T^3 d}{e}, \tag{14}$$

where k_f = 0.0258 W/(m·K) is the thermal conductivity of the fluid, $\sigma = 5.67{\cdot}10^{-8}$ W/(m²·K) is the Boltzmann constant, $d = 5{\cdot}10^{-5}$ m is the effective diameter of the pore, and ε = 0.95 is the emissivity. The specific heat capacity of wood (w); char (c); tar (t), and gas (g) are defined as a temperature function [13]: $C_{p,w}$ = 1500 + T J/(kg·K); $C_{p,c}$ = 420 + 2×T J/(kg·K); $C_{p,t}$ = -100 + 4×T J/(kg·K); $C_{p,g}$ = 770 + 0.63xT J/(kg·K). The initial temperature is set to $T_0 = 298\ K$. The thermal boundary conditions are illustrated in Figs. 4 and 5.

The diffusive heat transfer time constant $\tau_{3d} = \frac{L^2(\rho C_P)_{\mathrm{eff}}}{k_{\mathrm{eff}}} \approx 10^5$ s is much larger than the convective one $\tau_{3c} = \frac{\varepsilon L}{u_t} \approx 2.24$ s. This indicates that convective heat transfer plays a critical role in ensuring that thermal conditions suitable for carbonization, which occurs in a porous medium, are reached within practical timescales [14].

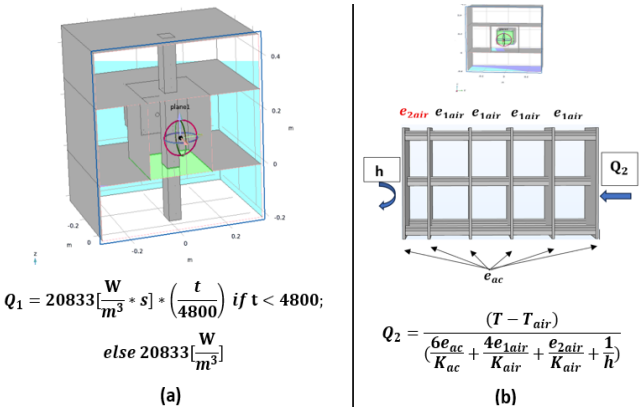

Fig. 4 – Thermal boundary conditions: (a) autothermal flux; (b) heat exchange between pyrolysis chamber and recovery system (steel plates and rods).

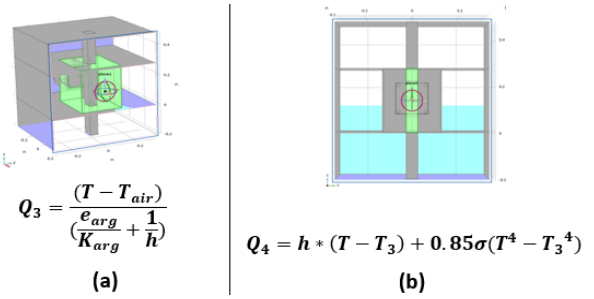

Fig. 5 – Thermal boundary conditions: Heat exchange between pyrolysis chamber and: (a) the insulating clay; (b) chimney.

The diffusive heat transfer time constant $\tau_{3d} = \frac{L^2(\rho C_P)_{\text{eff}}}{k_{\text{eff}}} \approx 10^5$ s is much larger than the convective one $\tau_{3c} = \frac{\varepsilon L}{u_t} \approx 2.24$ s. This indicates that convective heat transfer plays a critical role in ensuring that thermal conditions suitable for carbonization, which occurs in a porous medium, are reached within practical timescales [14].

3.1.5. DOMAIN ORDINARY DIFFERENTIAL EQUATIONS AND DIFFERENTIAL-ALGEBRAIC EQUATIONS (DODES AND DAES)

This interface allows you to define and solve custom equations locally. In this study, biomass decomposition is modeled using Arrhenius reaction rates, which describe the changes in wood (w) and char (c) over time.

$$\frac{\partial \rho_w}{\partial t} = S_w = -(k_t + k_g + k_c)\rho_w, \quad (15)$$

$$\frac{\partial \rho_c}{\partial t} = S_c = k_c \rho_w + k_{c2}\rho_t. \quad (16)$$

The initial solid mass distribution in the domain is set with wood density $\rho_{w,0} = 700 \frac{kg}{m^3}$, and char density $\rho_{c,0} = 0$. The characteristic time associated with the mass loss kinetics due to pyrolysis is given by: $\tau_4 = \frac{1}{(k_t + k_g + k_c)} \approx 10^2\ s$. This characteristic time indicates that the pyrolysis process under study proceeds as a relatively slow thermochemical reaction, even after the activation temperature is reached [15].

3.2. THE INSULATE CLAY LAYER

Thermal transfer in the solid material clay is modeled, considering conduction, internal heat sources, and boundary conditions. In transient regime, the equation is:

$$(\rho C_P)\frac{\partial T}{\partial t} + \nabla \cdot (-k\nabla T) = 0. \quad (17)$$

The initial temperature is set to $T_0 = 298$ K, and the applied boundary conditions are illustrated in Fig. 5. (a), including natural convection on the outer walls.

The characteristic time of the heat transfer in the clay is defined by $\tau_5 = \frac{L^2(\rho C_P)}{k} \approx 10^4$s indicating a slow diffusion of heat through the material. This high value suggests that clay provides effective thermal insulation by significantly slowing the propagation of heat.

3.3. THE CHIMNEY

To describe the physical phenomena occurring within the chimney, the Heat Transfer in Fluids interface is coupled with the Laminar Flow interface, which governs the fluid motion. Those equations are respectively:

$$(\rho_{air} C_{P,air})\left[\frac{\partial T}{\partial t} + (\mathbf{u_c} \cdot \nabla)T\right] + \nabla \cdot (-k_{air}\nabla T) = 0, \quad (18)$$

$$\boldsymbol{\rho_{air}}\left(\frac{\partial \mathbf{u_c}}{\partial t} + (\mathbf{u_c} \cdot \nabla)\mathbf{u_c}\right) = -\nabla p + \mu_{air}\nabla^2 \mathbf{u_c} + \mathbf{f}. \quad (19)$$

$$\mathbf{f} = \rho_{air}(1 - \beta_{air}(T - T_{\text{ref}}))\mathbf{g}, \quad (20)$$

The temperature at the chimney entrance is assumed to be equal to the ambient temperature. At the outer, we have outflow condition:

$$-\mathbf{n} \cdot \mathbf{q} = 0.$$

The characteristic times of diffusive and convection heat transfer are respectively: $\tau_{6d} = \frac{L^2 \rho_{air} C_{P,air}}{k_{air}} \approx 4 \cdot 10^3$ s and $\tau_{6c} = \frac{L}{u_c} = 1.36\ s.$ $\tau_{6c} \ll \tau_{6d}$. This suggests that the flow of pyrolysis gases in the chimney is dominated by convection driven by the thermosiphon effect [16].

3.4. THE HEAT RECOVERY SYSTEM

The heat transfer and solid mechanics are coupled to deformation caused by temperature changes in steel plates and rods. The equilibrium equation governs the quasi-static behavior of a solid subjected to thermomechanical loads:

$$\nabla \cdot \mathbf{S} = 0, \quad (21)$$

where **S** [Pa] is the stress tensor given by Hooke's law:

$$\mathbf{S} = C : (\frac{1}{2}[(\nabla \mathbf{u})^T + \nabla u] - \alpha(T - T_{ref})), \quad (22)$$

where C [Pa] is the elasticity tensor; α [$s^{-1}K^{-1}$] the linear thermal expansion coefficient, and **u** [m] is the displacement field.

- Initial condition: **u** = 0 (m); $\frac{\partial \mathbf{u}}{\partial t} = 0$ $\left(\frac{m}{s}\right)$;
- Boundary conditions: Fixed constraint for the exterior plate, **u** = 0 (m).

The same equation as (17) governs the heat transfer in the system. The boundary condition is shown in Fig. 4. (b). The characteristic time of this transfer $\tau_8 = \frac{L^2(\rho C_P)}{k} \approx 10^2$ s is relatively short, indicating that steel is a suitable material for heat recovery.

4. SIMULATION PARAMETERS AND COMPUTATIONAL PROCEDURE

We used a time step of 1 s, slightly below the smallest system time constant (1.36 s), to balance accuracy and efficiency. The simulation lasted 2 hours (7200 s) to monitor the process. Figure 6 illustrates the program workflow, encompassing preparation, solving, and analysis.

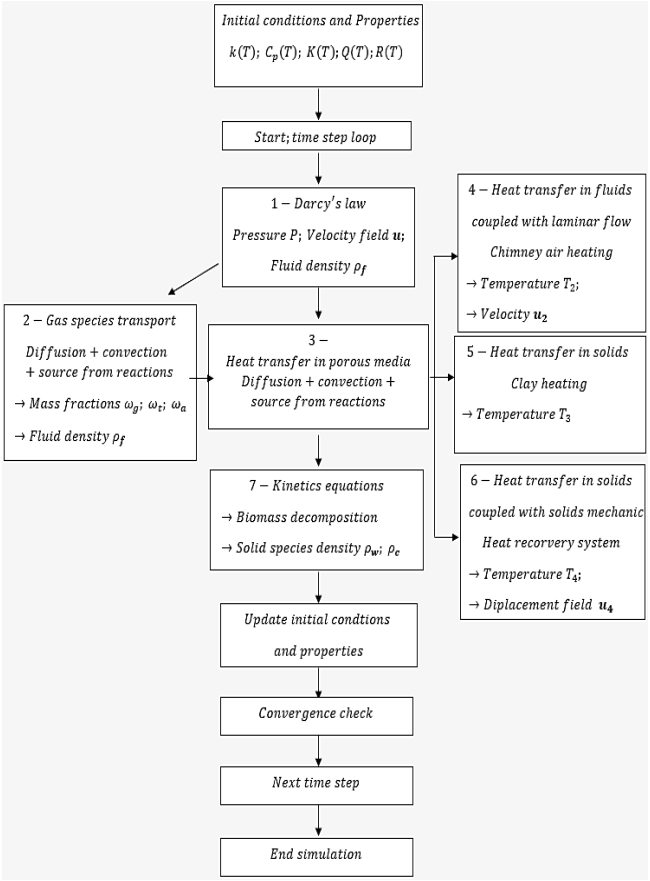

Fig. 6 – Diagram of the program execution procedure.

5. RESULTS AND DISCUSSION

5.1. PRESSURE AND TEMPERATURE DISTRIBUTION IN THE CARBONIZER

Figure 7 shows the pressure distribution in the pyrolysis chamber after 7200 s.

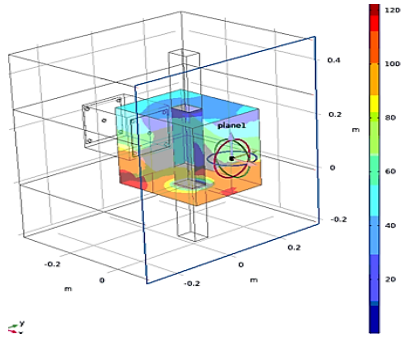

Fig. 7 – Pressure distribution in the pyrolysis chamber (red = 120 Pa, dark blue = 0 Pa) at t = 7200 s.

The pressure distribution within the carbonizer reveals localized high-pressure zones, mainly in the heating regions. The maximum local pressure is about 120 Pa relative to pressure. Finally, low-pressure zones (20 Pa) are found near the gas outlet openings, where the gases escape, indicating a natural decompression of the system [17]. At the same time, Darcy's velocity reaches a maximum of 0.002 m/s, with a corresponding maximum temperature of 800 K. Gas generation during carbonization serves as a mass source in the porous medium, thereby increasing fluid density and causing a pressure rise under constant-volume conditions [18].

The pyrolysis gases, as they exit toward the chimney, heat up the fluid flowing through it. Figure 8 illustrates the temperature distribution within the chimney at t = 7200 s.

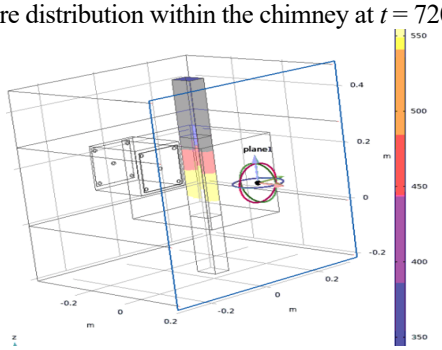

Fig. 8 – Temperature distribution in the chimney (Yellow = 550 K, purple = 350 K) at t = 7200 s.

The hottest area, reaching approximately 550 K, is located near the pyrolysis zone, also known as the main reaction area. On the other hand, cooler regions, with temperatures around 350 K, are farther from the heat source at the outer edge of the chimney. The outlet temperature of 350 K can still be beneficial for applications such as preheating air or biomass to enhance the pyrolysis process [19], or for drying and other low-temperature processes. At 3600 s, the temperature reaches approximately 660 K throughout much of the pyrolysis chamber as shown in Fig. 9.

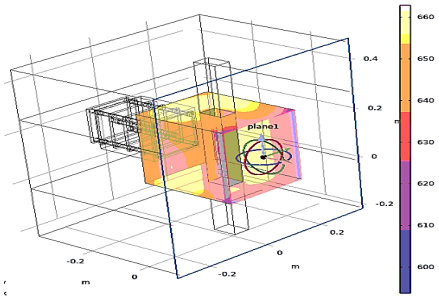

Fig. 9 – Temperature distribution in the pyrolysis chamber (Yellow = 660 K, purple = 350 K) at t = 3600 s.

Figure 9 shows a thermal equilibrium at above 660 K due to an advanced stage of pyrolysis, with cellulose and hemicellulose nearly fully decomposed. The temperature rise then slows, reaching about 770 K at 7200 s, due to the depletion of reactive components and the slower, less exothermic degradation of lignin [20].

5.2. THERMO-MECHANICAL ANALYSIS OF THE PLATE-AND-ROD HEAT RECOVERY STRUCTURE

Following the carbonizer simulation, the average temperature on the directly connected steel plate was evaluated and expressed as a polynomial function of time:

$$T(t) = 313\ [\mathrm{K}] + 0.07\left[\frac{\mathrm{K}}{s}\right]\cdot t + 4.82\cdot 10^{-8}\left[\frac{\mathrm{K}}{s^2}\right]\cdot t^2 - 6.687\cdot 10^{-12}\left[\frac{\mathrm{K}}{s^3}\right]\cdot t^3.$$

The temperature and von Mises stress distribution in the heat recovery system at 7200 s are shown in Fig. 10.

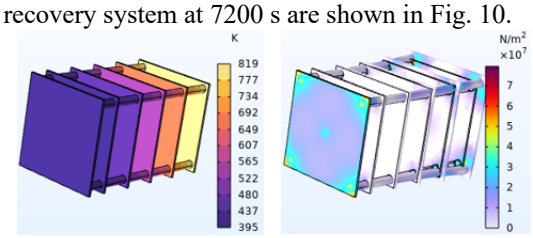

(a) **(b)**

Fig. 10 – (a) Temperature distribution in heat recovery system at t = 7200 s (yellow = 819 K, violet = 395 K); (b) Von Mises Stress distribution in heat recovery system at t = 7200 s (white = 0 N/m², red = 6.81 ·10^7 N/m²).

A thermal gradient forms from the first to the sixth plate, with temperatures decreasing from 819 K to 395 K. On the sixth plate, temperatures reach up to 410 K at the rod contacts and drop to 395 K at the coolest point, making it suitable for thermoelectric use. The highest stresses are concentrated at the corners of the sixth heated plate, reaching a maximum of 6.81·10^7 N/m^2. This is due to the mechanical anchoring designed for the thermoelectric generator. This maximum stress remains well below the steel's yield strength of approximately 25·10^7 N/m² [21], indicating the system's long-term durability.

Figure 11 illustrates the evolution of the average temperature on the first and sixth plates during the 7200 s process, in a configuration where the first five plates are spaced 5 cm apart.

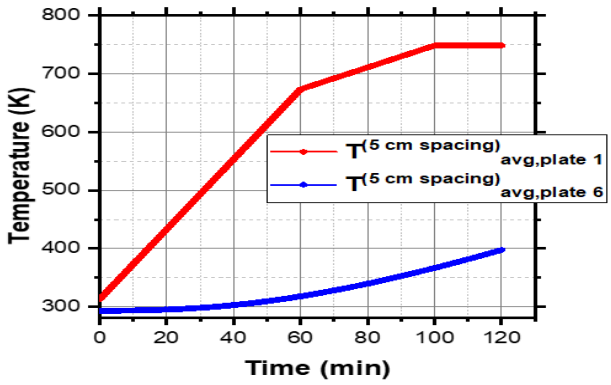

Fig. 11 – Average temperature evolution on plates 1 and 6 (5 cm spacing configuration).

The first plate, directly exposed to the heat flux, quickly reaches about 750 K after 60 minutes and then stabilizes up to 120 minutes, a behavior consistent with findings by Dhaundiyal and al. during acacia wood pyrolysis [22]. In contrast, the sixth plate, located at the opposite end, heats up more slowly and reaches approximately 400 K after 120 minutes, indicating a delay in heat transfer through the system.

This temperature is suitable for bismuth telluride thermoelectric modules, which can withstand temperatures up to 360 °C (633 K). However, since it's well below the limit, other configurations could improve performance. For instance, replacing the plates with a 23 cm steel bar would raise the temperature to approximately 680 K (based on simulations). Still, it would increase the system's weight by a factor of 12 and exceed the module's thermal limit.

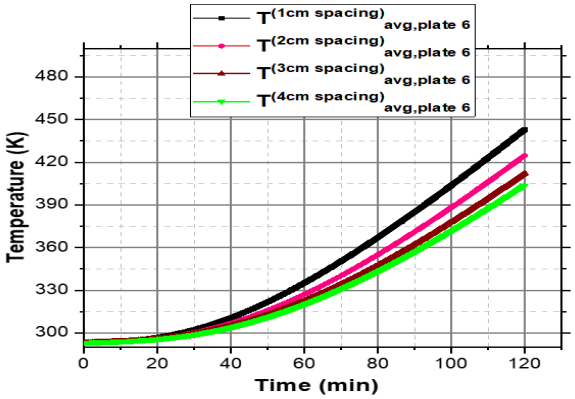

Fig. 12 – Average temperature evolution on plate 6 (1 cm; 2 cm; 3 cm and 4cm spacing configuration).

A better option is to optimize the plate spacing to enhance heat transfer while maintaining a lightweight and safe system. During the initial setup, the first and middle four plates were spaced 5 cm apart. The sixth plate remains fixed at the end, but the distances between the first plate (near the pyrolysis chamber) and the four middle plates will be adjusted to 1 cm, 2 cm, 3 cm, and 4 cm, respectively. Figure 12 shows the average temperature on the sixth plate for those configurations.

The graph shows that the closer the first five plates are, the faster the sixth plate heats up. With a spacing of 1 cm, the temperature reaches 443 K after 120 min, compared to 424 K, 412 K, and 403 K for spacings of 2, 3, and 4 cm, respectively. This trend is due to more efficient heat conduction when the plates are closer together, allowing better heat recovery from the pyrolysis chamber and its transfer to the sixth plate (located at the outer end) through the five metal rods. Figure 13 shows the variation of maximum temperature (blue bar) and maximum von Mises stress (red curve) of the sixth plate as a function of the spacing.

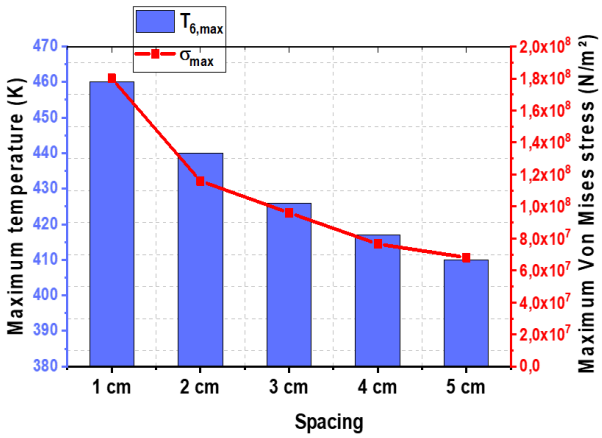

Fig. 12 – Maximum temperature and maximum Von Mises stress on Plate 6 (1 cm; 2 cm; 3 cm; 4 cm and 5 cm spacing configuration).

As spacing increases from 1 cm to 5 cm, the sixth plate's maximum temperature drops from 467 K to 400 K, and the Von Mises stress falls more sharply from 1.8·10^8 Pa to 6.8·10^7 Pa. This indicates reduced thermal expansion and mechanical stress. A 2 cm spacing offers the best balance between high temperature and moderate stress.

5.3. OUTPUT POWER AND MATCHED LOAD RESISTANCE OF SEEBECK MODULE

We plan to use the TEG1-PB-12611-6.0 module (TECTEG MFR), which supports temperatures up to 633 K and delivers approximately 9.5 W under ideal conditions. Manufacturer data helped estimate power and optimal resistance as a function of hot-side temperature (with the cold side at 303 K) [5].

$$P(T) = -10.9474\,[\mathrm{W}] + 0.0902\left[\frac{\mathrm{W}}{\mathrm{K}}\right]\cdot T - 2.907\cdot 10^{-4}\left[\frac{\mathrm{W}}{\mathrm{K}^2}\right]\cdot T^2 + 3.6875 * 10^{-7}\left[\frac{\mathrm{W}}{\mathrm{K}^3}\right]\cdot T^3$$

$$R_{load}(T) = -1.0878\,[\Omega] + 0.0101\left[\frac{\Omega}{\mathrm{K}}\right]\cdot T - 2.0837\cdot 10^{-5}\left[\frac{\Omega}{\mathrm{K}^2}\right]\cdot T^2 + 1.5923\cdot 10^{-8}\left[\frac{\Omega}{\mathrm{K}^3}\right] * T^3.$$

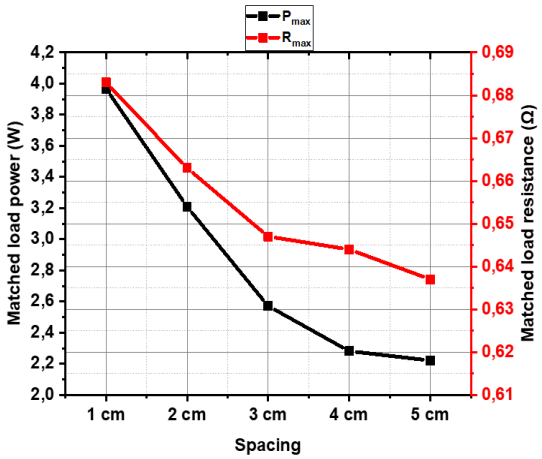

Fig. 13– Matched load output power and matched load resistance for TEG (1 cm; 2 cm; 3 cm; 4 cm and 5 cm spacing configuration).

Within the studied temperature range, the maximum electrical power generated by the thermoelectric module increases significantly with the hot-side temperature, rising from about 2.221 W to 3.968 W as the spacing decreases from 5 cm to 1 cm. The optimal load resistance also increases slightly, from 0.633 Ω to 0.699 Ω, reflecting the temperature's influence on the module's properties.

8. CONCLUSION

This study has enabled a numerical investigation not only of the pyrolysis process of wood chips in a parallelepiped carbonizer but also of the feasibility of efficiently harnessing the thermal energy generated. The results indicate that the hot air exiting the chimney reaches a temperature of aropproximately50 K, making it suitable for hot-air drying applications or for preheating the mass before carbonization. Moreover, the maximum temperature recorded on the hot side of the sixth steel plate (intended to support a thermoelectric module) can reach up to 443 K. Under these conditions, the selected TEG1-PB-12611-6.0 module can deliver a maximum electrical power of approximately 3.97 W. These findings confirm the potential for integrating energy recovery solutions into pyrolysis systems, particularly for decentralized applications in rural areas.

ACKNOWLEDGMENTS

The first author expresses his deep gratitude for the financial support of the Agence Universitaire de la Francophonie (AUF), which made this research possible. We thank the Laboratory of Conversion and Energy Sources and the Multiphysics Modeling Laboratory of the Faculty of Electrical Engineering at the National University of Sciences and Technology Politehnica of Bucharest for their valuable collaboration and indispensable technical resources.

Received on …

Credit authorship contribution statement

Author_1: Writing, numerical simulation.
Author_2: Proposed the idea for the simulation model, numerical simulation data analysis.
Author_3: Physical-mathematical overview, numerical simulation data analysis.

REFERENCES

1. P. Sun, H. Peng, *Valorisation of biomass waste for sustainable Valorisation of biomass waste for sustainable bioenergy and biofuel production,* Bioengineering, **10**, *5,* pp. 4–7, (2023).
2. C. Xia, L. Cai, H. Zhang, L. Zuo, S. Q. Shi, and S. S. Lam, *A review on the modeling and validation of biomass pyrolysis with a focus on product yield and composition,* Biofuel Research Journal, **29**, *1,* pp. 1296–1315, (2021).
3. J. Erkmen, H. Ibrahim, E. Kavci, and M. Sari, *A new environmentally friendly insulating material designed from natural materials,* Construction and Building Materials, **255,** *1,* pp. 119357–119364, (2020).
4. L.M. Grajeda, L.M.Thompson, W. Arriaga, E. Canuz, S.B. Omer, M. Sage, E.A. Baumgartner, J.P. Bryan, J.P. McCracken, *E ff ectiveness of gas and chimney biomass stoves for reducing household air pollution pregnancy exposure in Guatemala : sociodemographic effect modifiers,* Environmental Research and Public Health, **17,** *21,* pp. 7723–7736, (2020).
5. A. Anitha Angeline and J. Jayakumar, *Analysis of (Bi2Te3-PbTe) hybrid thermoelectric generator for effective power generation, Int. Conf. Innov. Information, Embed. Commun. Syst. (ICIIECS),* Karpagam College of Engineering in Coimbatore, Tamil Nadu, India, 2015.
6. O. Üner, Y. Bayrak, *The effect of carbonization temperature, carbonization time and impregnation ratio on the properties of activated carbon produced from Arundo donax,* Microporous Mesoporous Mater., **268,** *1,* pp. 225-234, (2018).
7. M.W. Seo, H.M. Jeong, W.J. Lee, S.J. Yoon et al, *Carbonization characteristics of biomass/coking coal blends for the application of bio-coke,* Chem. Eng. J., **394,** *1,* pp. 124943–124952, (2020).
8. F. Shafizadeh, P.P.S. Chin, *Thermal deterioration of wood,* Wood Technol. Chem. Asp., **43,** *1,* pp. 57–81, (1977).
9. C. Di Blasi, *Modeling Intra- and Extra-Particle Processes of Wood Fast Pyrolysis,* AIChE J., **48,** *10,* pp. 2386–2397, (2002).
10. W.C. Park, A. Atreya, H.R. Baum, *Experimental and theoretical investigation of heat and mass transfer processes during wood pyrolysis,* Combust. Flame, **157,** *3,* pp. 481–494, (2010).
11. J.S. Tumuluru, S. Sokhansanj, J.R. Hess, C.T. Wright, R.D. Boardman, *A review on biomass torrefaction process and product properties for energy applications,* Industrial Biotechnology, **7,** *5,* pp. 384–401, (2011).
12. L. Chen, H. Feng, Z. Xie, F. Sun, *"Disc-point" mass transfer constructal optimizations with Darcy and Hagen-Poiseuille flows in porous media,* Appl. Math. Model., **38,** *4,* pp. 1288–1299, (2014).
13. M. G. Gronli, M. C. Melaaen, *Mathematical model for wood pyrolysis-comparison of experimental measurements with model predictions,* Energy and Fuels, **14,** *4,* pp. 791–800, (2000).
14. I.A. Badruddin, Azeem, T.M. Yunus Khan, M.A. Ali Baig, *Heat Transfer in Porous Media: A Mini Review,* Mater. Today Proc., **24,** *1,* pp. 1318–1321, (2020).
15. R. B. Bates and A. F. Ghoniem, *Modeling kinetics-transport interactions during biomass torrefaction: The effects of temperature, particle size, and moisture content,* Fuel, **137,** *1,* pp. 216–229, (2014).
16. H. Ma, L. He, G. Yu, Z. Yu, *Natural convection heat transfer and fluid flow in a thermal chimney with multiple horizontally-alighned cylinders,* Int. J. Heat Mass Transf., **183,** *1,* (2022).
17. B. Liu, X. Liu, C. Lu, A. Godbole, G. Michal, L. Teng, *Decompression of hydrogen—natural gas mixtures in high-pressure pipelines: CFD modelling using different equations of state,* Int. J. Hydrogen Energy, **44,** *14,* pp. 7428–7437, (2019).
18. K.P. Keboletse. F. Ntuli, O.P. Oladijo, *Influence of coal properties on coal conversion processes-coal carbonization, carbon fiber production, gasification and liquefaction technologies : a review,* Int. J. Coal Sci. Technol., **8,** *5,* pp. 817–843, (2021).
19. M.A. Abdullah, *Improvement of the pyrolysis system by integrating solar energy-based preheating system,* IOSR J. Mech. Civ. Eng. (IOSR-JMCE), **18,** *3,* pp. 25–30, (2021).
20. J. López-Beceiro, A. M. Díaz-Díaz, A. Álvarez-García, J. Tarrío-Saavedra, S. Naya, *The complexity of lignin thermal degradation in the isothermal context,* Processes, **9,** *7,* (2021).
21. N. Pervan, E. Mešić, and M. Čolić, *Stress analysis of external fixator based on stainless steel and composite material,* Int. J. Mech. Eng. Technol., **8,** *1,* pp. 189–199, (2017).
22. A. Dhaundiyal, S.B. Singh, I. Bacskai, *Mathematical modelling of pyrolysis of hardwood (acacia),* Acta Technol. Agric., **23,** *4*, pp. 176–182, (2020).
23. ***Comsol Multiphysics,* v.6.3.